Nano-Micro Lett. (2016) 8(2):174–181
DOI 10.1007/s40820-015-0075-z

ARTICLE

Facile Synthesis of Porous Zn–Sn–O Nanocubes and Their Electrochemical Performances

Bo Li[1] · Xiaomin Li[1] · Jiantao Zai[1] · Xuefeng Qian[1]

Received: 31 August 2015 / Accepted: 27 October 2015 / Published online: 21 December 2015

Abstract Porous Zn–Sn–O nanocubes with a uniform size were synthesized through a facile aqueous solution route combined with subsequent thermal treatment. The chemical composition, morphology, and microstructure of Zn–Sn–O nanocubes, which have significant effects on the lithium storage performances, were easily tuned by adjusting the calcination temperature in preparation processes of $ZnSn(OH)_6$ solid nanocubes. Further studies revealed that porous Zn–Sn–O nanocubes prepared at 600 °C exhibited a good rate capability and a high reversible capacity of 700 mAh g^{-1} at a current density of 200 mA g^{-1} after 50 cycles, which may be a great potential as anode materials in Lithium-ion batteries.

Keywords Zn–Sn–O · Nanocubes · Porous · Lithium-ion batteries

1 Introduction

Lithium-ion batteries (LIBs), currently as versatile power sources for various portable electronics, are now considered for applications in electric or hybrid electric vehicles [1–6]. Such applications require LIBs of high power, high energy density, long cycle life, excellent safety, low toxicity, and low cost [1, 7, 8]. To meet these requires, a great deal of efforts have been made to take a further step in anode electrode materials with superior performances [9–15]. Among various developed anode materials, Sn-based oxide compounds, including SnO_2, $ZnSnO_3$, $CoSnO_3$, Zn_2SnO_4, and so on, have attracted an extensive attention as potential substitutes for graphite anodes because of their higher theoretical capacity [16–21]. Unfortunately, the practical application of Sn-based oxide anode materials is usually hindered by drastic volume change of 300 % during Li^+ insertion/extraction process, which results in very rapid capacity decay and pulverization of electrodes [7, 16, 22, 23]. Fabrication of porous nanostructures is one of the most effective methods to solve the problem and improve the cycle performance, because the local empty space in porous structures can partially accommodate the large volume change [24, 25]. In past few years, porous nanostructures based on Sn-based oxides were usually prepared through chemical vapor deposition, hydrothermal reaction, hard or soft template method, and so on [26–30].

Although the electrochemical performances of porous Sn-based oxide anodes have been improved a lot, the preparation procedures are usually complicated and costly. It is still a challenge to explore a facile approach for fabricating porous Sn-based oxide anode materials with controllable morphology and good electrochemical properties for practical applications. Herein, porous Zn–Sn–O nanocubes with different morphology and microstructure were synthesized by sintering $ZnSn(OH)_6$ solid nanocubes at different temperatures. The obtained porous Zn–Sn–O nanocubes exhibited high reversible capacity and good rate capability.

✉ Jiantao Zai
zaijiantao@sjtu.edu.cn

✉ Xuefeng Qian
xfqian@sjtu.edu.cn

[1] School of Chemistry and Chemical Engineering and State Key Laboratory of Metal Matrix Composites, Shanghai Jiao Tong University, Shanghai 200240, People's Republic of China

2 Experimental Section

2.1 Synthesis of Porous Zn–Sn–O Nanocubes

In a typical procedure, 2.876 g of $ZnSO_4 \cdot 7H_2O$ was dissolved into 150 mL deionized water, and then 2.848 g of $Na_2SnO_3 \cdot 4H_2O$ was added under continuous stirring at room temperature. After stirring for 5 h, the resulted white precipitation was collected by centrifuging, washing with deionized water for several times, and drying in air at 80 °C. Finally, porous Zn–Sn–O nanocubes were obtained by sintering the as-prepared white precursors at respective 500, 600, and 700 °C for 2 h in air with a heating rate of 1 °C min^{-1}.

2.2 Characterizations

Morphology of the obtained products was characterized by field emission scanning electron microscope (FESEM, JSM-7401F) and transmission electron microscope (TEM, JEOL, JEM-2100). Powder X-ray diffraction (XRD) was recorded on a Shimadzu XRD-6000 with Cu-Kα radiation, in which the voltage and current of X-ray tube are of 40 kV and 30 mA, respectively. Thermogravimetric analysis (TGA) was performed on a SDT Q600 thermoanalyzer (DSC-TGA, TA, USA) in air. The specific surface area and pore size distribution were measured by a NOV A2200e analyser (Quantachrome, USA).

2.3 Electrode Fabrication

Working electrode was fabricated as follows: First, porous Zn–Sn–O nanocubes (70 wt%), Super-P carbon black (15 wt%), and sodium carboxymethyl cellulose (CMC, 15 wt%) were mixed in water to form a slurry. Then, the slurry was spread onto a Cu foil by a doctor blade method, followed by drying in vacuum at 80 °C for 8 h. A lithium foil acted as both the counter electrode and reference electrode, and a microporous polypropylene membrane (Celgard 2500) was used as separator. Then, CR2016 coin cells were assembled in an argon-filled glove box with moisture and oxygen contents below 1 ppm. The electrolyte was 1 M of $LiPF_6$ in the mixture of ethylene carbonate (EC)/dimethyl carbonate (DMC) (1:1 vol%). Charge–discharge cycles of cells were measured between 0.01 and 2.0 V versus Li^+/Li using a battery test instrument (LAND CT2001A model, Wuhan Jinnuo Electronics, China) at room temperature. Cyclic voltammetry (CV) was conducted on the workstation at a scan rate of 0.1 mV s^{-1} in a potential range of 5 mV–2.0 V (vs. Li/Li^+).

3 Results and Discussion

Figure 1 displays the XRD pattern, TGA curve, FESEM, and TEM images of $ZnSn(OH)_6$ precursors. From Fig. 1a, one can see that all of the diffraction peaks of the as-

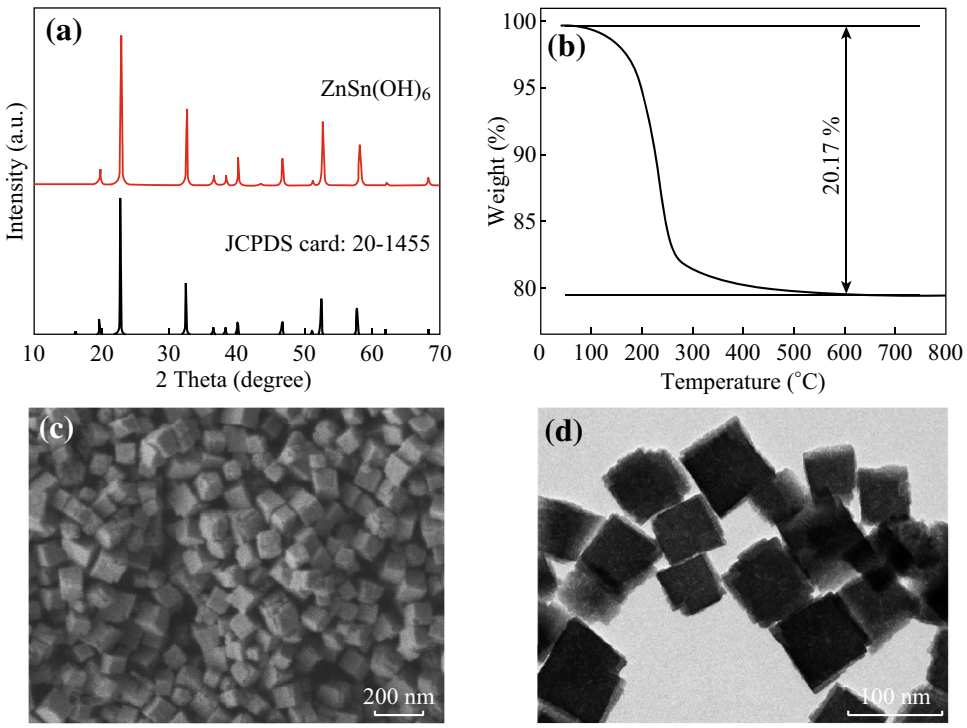

Fig. 1 **a** XRD pattern, **b** TGA curve, **c** FESEM, and **d** TEM image of the as-prepared $ZnSn(OH)_6$

prepared products are in good agreement with the cubic phase of $ZnSn(OH)_6$ (JCPDS CARD No. 20-1455). The sharp peaks imply that the obtained $ZnSn(OH)_6$ particles have good crystallinity, and no impurity phases were observed. Figure 1b shows the TGA curve of $ZnSn(OH)_6$, heating from 30 to 800 °C in air at a rate of 10 °C min^{-1}. The first weight loss (about 1 %) occurs in the temperature range of 30–100 °C, corresponding to the removal of water and the residual organic molecular absorbed on samples. The second weight loss (20.17–1 % = 19.17 %) at high temperature (100–500 °C) is ascribed to the loss of three water molecules according to the following chemical formula:

$$ZnSn(OH)_6 \rightarrow ZnSnO_3 + 3H_2O \quad (1)$$

The theoretical weight loss based on the above formula is about 18.9 %, which is consistent with the experimental result. The SEM image (Fig. 1c) shows that the obtained $ZnSn(OH)_6$ is composed of uniform and monodisperse nanocubes with side length of 80–120 nm. The TEM image suggests that the as-prepared $ZnSn(OH)_6$ nanocubes are in solid morphology (Fig. 1d).

The as-prepared $ZnSn(OH)_6$ nanocubes were annealed at 500, 600, and 700 °C for 2 h, and the calcinated products are marked as Zn–Sn–O-500, Zn–Sn–O-600, and Zn–Sn–O-700, respectively. From the XRD patterns of products calcined at different temperatures (Fig. 2), it can be seen that only one broad peak is observed for Zn–Sn–O-500, suggesting the amorphous nature of the products prepared at 500 °C. When the calcination temperature is 600 °C, three diffraction peaks of SnO_2 (JCPDS CARD No. 41-1445) appear for Zn–Sn–O-600, indicating a phase transition from amorphous to crystalline. However, the intensity of these peaks is very weak due to the poor crystallinity or some amorphous crystallites of Zn–Sn–O-600. Characteristic peaks of SnO_2 and spinal Zn_2SnO_4 (JCPDS CARD No. 24-1470) appear for Zn–Sn–O-700 when the calcination temperature was further increased to 700 °C. Considering these facts, the thermal process of

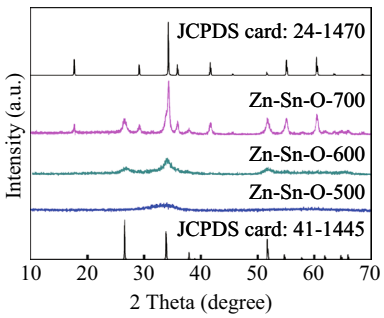

Fig. 2 XRD patterns of Zn–Sn–O-500, Zn–Sn–O-600, and Zn–Sn–O-700

$ZnSn(OH)_6$ sintered at different temperatures can be proposed as follows:

$$500\ ^\circ C:\ ZnSn(OH)_6 \rightarrow\ ZnSnO_3(\text{amorphous}) + 3H_2O, \quad (2)$$

$$600\ ^\circ C:\ 2ZnSnO_3(\text{amorphous}) \rightarrow\ Zn_2SnO_4(\text{amorphous}) + 2SnO_2(\text{crystalline}), \quad (3)$$

$$700\ ^\circ C:\ Zn_2SnO_4(\text{amorphous}) + SnO_2(\text{crystalline}) \rightarrow\ Zn_2SnO_4(\text{crystalline}) + SnO_2(\text{crystalline}) \quad (4)$$

When sintering at 500 °C, $ZnSn(OH)_6$ lost three water molecules to form amorphous $ZnSnO_3$. At 600 °C, amorphous $ZnSnO_3$ decomposed into amorphous Zn_2SnO_4 and crystalline SnO_2. With calcination temperature further increasing to 700 °C, the state of Zn_2SnO_4 transferred from amorphous to crystalline.

The morphology and microstructure of the porous Zn–Sn–O nanocubes prepared at different calcination temperatures are shown in Fig. 3. When the as-prepared $ZnSn(OH)_6$ nanocubes were calcined at 500 °C, the morphology of Zn–Sn–O-500 (Fig. 3a) is similar to that of $ZnSn(OH)_6$ precursors (Fig. 1c). After treated at 600 °C, a basic shape of nanocubes can also be maintained (Fig. 3c, Zn–Sn–O-600), whereas some uniform holes on/in the surface or body were formed (Fig. 3d). However, as the temperature increased to 700 °C, the morphology of products became irregular and large holes were observed (Fig. 3e, Zn–Sn–O-700). The formation of porous structure may be due to the removal of water during the thermal decomposition processes.

Figure 4 shows the N_2 adsorption/desorption isotherm curves and porous volume distribution of Zn–Sn–O samples. The isotherms have a characteristic of a type IV with type H3 hysteresis loop, indicating their mesoporous microstructure [31, 32]. The BET surface areas of Zn–Sn–O-500, Zn–Sn–O-600, and Zn–Sn–O-700 are calculated to be 31.64, 40.01, and 21.89 $m^2\ g^{-1}$, respectively. The pore size distribution of Zn–Sn–O-500 calculated from the BJH method is in a bimodal nature with a narrow distribution of pore size centered at 3 nm and a wide distribution of pore size centered at 20 nm. Zn–Sn–O-600 has a relatively narrow distribution of pore size centered at 6 nm, indicating a high-uniform pore structure. However, Zn–Sn–O-700 has a wide distribution of pore size centered at 40 nm.

The properties of the porous Zn–Sn–O nanocubes with different crystallinity, chemical composition, and microstructure as an anode material for LIBs were further studied. To identify the lithium storage mechanism of the porous Zn–Sn–O nanocubes, the cyclic voltammetry of Zn–Sn–O-600 was carried out in the voltage range of

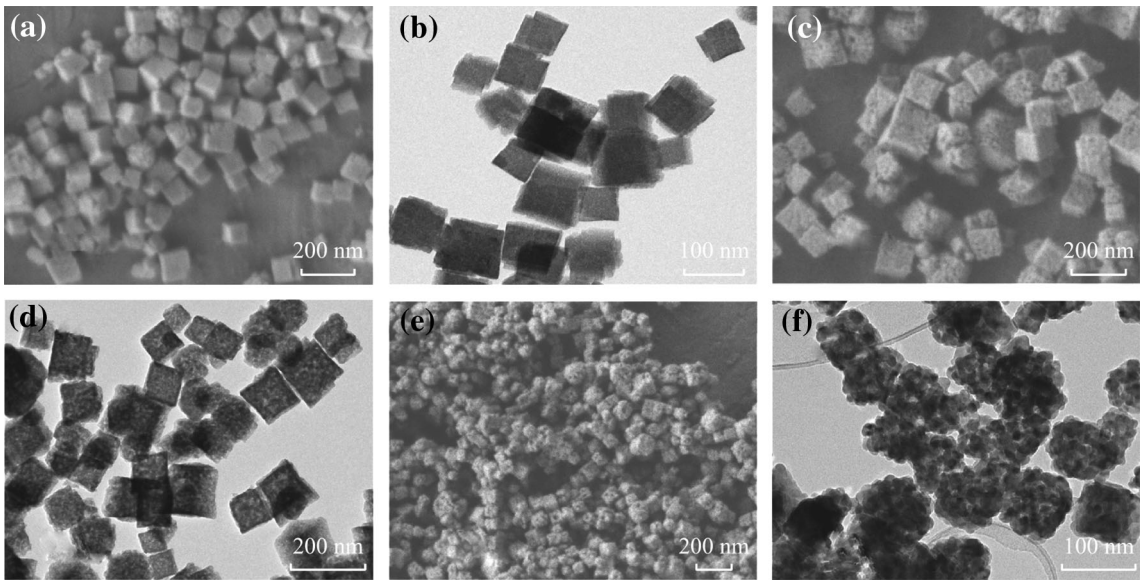

Fig. 3 FESEM images and TEM images of porous Zn–Sn–O nanocubes: **a**, **b** Zn–Sn–O-500, **c**, **d** Zn–Sn–O-600, and **e, f** Zn–Sn–O-700

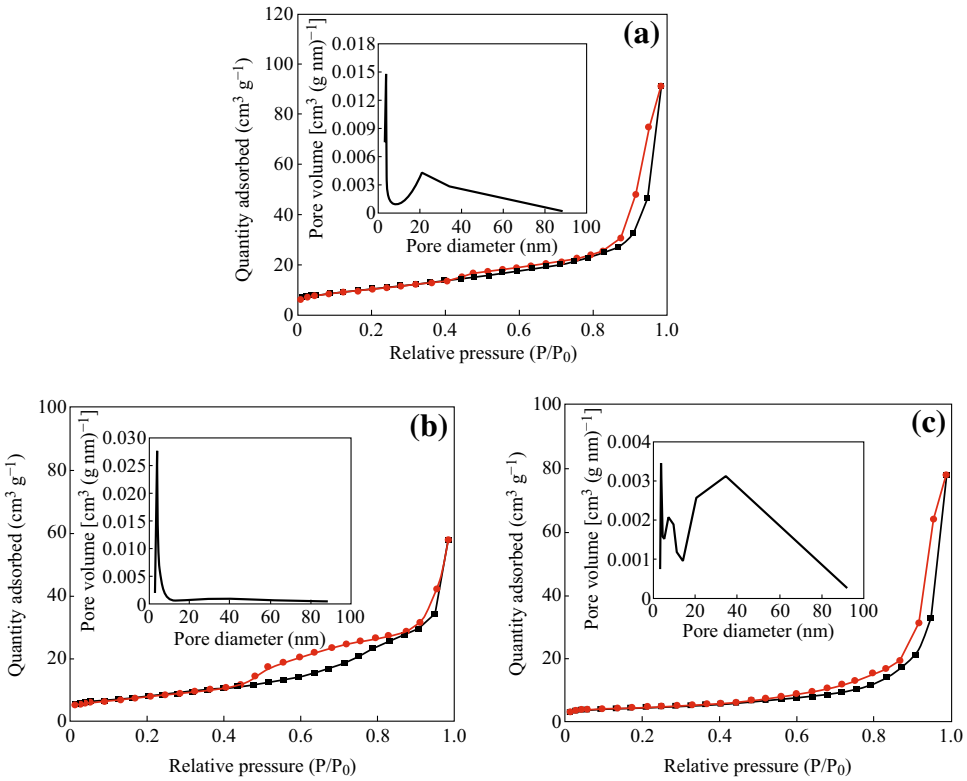

Fig. 4 N_2 adsorption/desorption isotherm curves and porous volume distribution of the Zn–Sn–O: **a** Zn–Sn–O-500, **b** Zn–Sn–O-600, and **c** Zn–Sn–O-700

0.01–2 V (see Fig. 5a). Based on the lithium storage mechanism of SnO_2 [16], ZnO [33], and Zn_2SnO_4 [34], a lithium insertion mechanism of Zn–Sn–O-600 nanocubes is proposed as follows:

$$Zn_2SnO_4 + 8Li^+ + 8e^- \rightarrow Sn + 2Zn + 4Li_2O \quad (5)$$

$$SnO_2 + 4Li^+ + 4e^- \rightarrow Sn + 2Li_2O \quad (6)$$

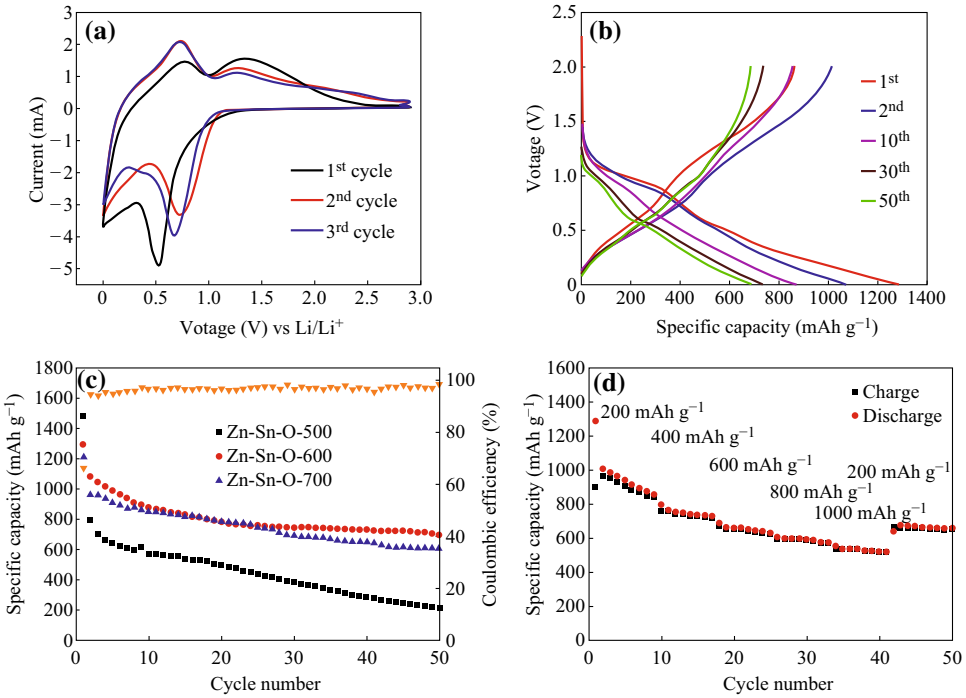

Fig. 5 **a** CV curves of Zn–Sn–O-600 electrode for the first three cycles in the voltage range of 0.01–2.0 V at scan rate of 0.1 mV s^{-1}; **b** Charge–discharge profile of Zn–Sn–O-600 electrode for the first three cycles in the voltage range of 0.01–2.0 V at a current density of 200 mA g^{-1}; **c** The cycling performances of the porous Zn–Sn–O nanocubes prepared at different calcination temperatures at a current density of 200 mA g^{-1} between 0.01 and 2.0 V; **d** Rate performances of Zn–Sn–O-600

$$\mathrm{Sn} + x\mathrm{Li}^+ \leftrightarrow \mathrm{Li}_x\mathrm{Sn} \quad (0 \le x \le 4.4) \tag{7}$$

$$\mathrm{Zn} + y\mathrm{Li}^+ \leftrightarrow \mathrm{Li}_y\mathrm{Zn} \quad (y \le 1) \tag{8}$$

In the first cycle for Zn–Sn–O-600 (Fig. 5a), two cathodic peaks, located at 0.53 and 0.05 V, correspond to the multistep electrochemical lithiation process with the decomposition of Zn_2SnO_4 and SnO_2 (Eqs. 5 and 6) and the formation of alloys (Eqs. 7 and 8). Meanwhile, the anodic peak at 0.63 V corresponding to the dealloying reaction and a broad anodic peak at ~1.35 V are attributed to the oxidation of Sn (1.3 V) and Zn (1.5 V).

Figure 5b depicts the charge/discharge voltage profiles of the 1st, 2nd, 10th, 30th, and 50th cycle for the porous Zn–Sn–O-600 nanocubes cycled between 0.01 and 2.0 V at a current density of 200 mA g^{-1}. The initial discharge and charge capacities are about 1290 and 860 mAh g^{-1}, respectively. The large capacity loss in the first cycle is mainly attributed to the initial irreversible formation of Li_2O and inevitable formation of a solid electrolyte interface (SEI) layer as well as additional reaction from conducting agent, which is common for most anode materials [35–38]. Figure 5c shows the cycling performances of the as-prepared porous Zn–Sn–O nanocubes. The initial discharge capacities are about 1470 (Zn–Sn–O-500), 1290 (Zn–Sn–O-600), and 1230 (Zn–Sn–O-700) mAh g^{-1} at the current density of 200 mh g^{-1}. However, the discharge capacity of Zn–Sn–O-500 exhibits a rapid decline, and Zn–Sn–O-700 just maintains 590 mAh g^{-1} after 50 cycles, while Zn–Sn–O-600 can keep around 700 mAh g^{-1}. These results indicate that Zn–Sn–O-600 has a better capacity and cycling performance. To evaluate the rate capability of the obtained products, porous Zn–Sn–O-600 nanocubes are cycled at various current densities ranging from 200 to 1000 mA g^{-1}. From Fig. 5d, one can see that only small capacity decreases as the current density increasing, and a stable reversible capacity of 538 mAh g^{-1} can be maintained even at a high current density of 1000 mA g^{-1}. When the current density returns to 200 mA g^{-1}, stable reversible capacity of 663 mAh g^{-1} can be restored for Zn–Sn–O-600, indicating the stability of the porous Zn–Sn–O anode materials.

The improved electrochemical performances of the obtained porous Zn–Sn–O nanocubes could be attributed to their unique nanostructures. Firstly, the void space provided by porous structure can mitigate the volume change effect during the repeated charge–discharge cycling process, leading to enhanced capacity retention. Meanwhile, the narrow pore size and high specific surface area are beneficial to even the electrolyte diffusion and shorten the transport distance of Li^+ ions, which is benefit for the rate capability [39]. Furthermore, the in situ hybridization of amorphous Zn_2SnO_4 and crystalline SnO_2 in Zn–Sn–O-600

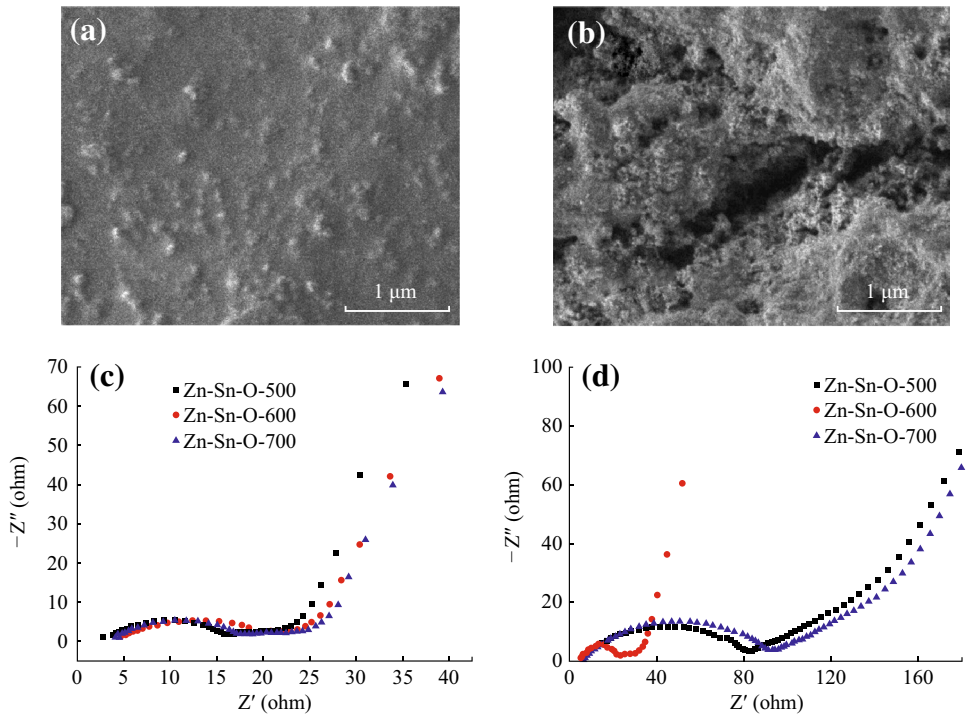

Fig. 6 Surface morphology of the electrodes after 50 cycles: **a** Zn–Sn–O-600 and **b** Zn–Sn–O-700. EIS spectra of Zn–Sn–O-500, Zn–Sn–O-600, and Zn–Sn–O-700 electrodes: **c** after the first cycle, and **d** after 50 cycles

may also contribute to their lithium storage performance because the volume change upon cycling can be partly mitigated in an isotropic loose dense structure [18]. The morphology of the electrode after 50 cycles was monitored using SEM images. From which, one can see that Zn–Sn–O-600 still maintains unbroken with no significant cracks or delaminations (Fig. 6a), while some cracks were observed on the surface of Zn–Sn–O-700 (Fig. 6b), indicating that the electrode structure of Zn–Sn–O-600 is more stable over the repeated cycling processes. To provide further evidence, Fig. 6c, d displays the EIS spectra of Zn–Sn–O-500, Zn–Sn–O-600, and Zn–Sn–O-700 electrodes. The resistance of the three electrodes shows little difference after the first cycle (Fig. 6c). However, the Zn–Sn–O-500 and Zn–Sn–O-700 electrodes exhibit evident impedance changes after 50 cycles (Fig. 6d). In contrast, a very slight change in the resistance of the Zn–Sn–O-500 electrode is observed after 50 cycles, confirming the excellent structural stability of the composite upon cycling.

4 Conclusions

In summary, a facile, low-cost, and scalable process was developed to synthesize porous Zn–Sn–O nanocubes. The chemical composition, morphology, and microstructure of Zn–Sn–O nanocubes were easily controlled by adjusting the calcination temperature. Electrochemical evaluation reveals that the porous Zn–Sn–O nanocubes prepared at 600 °C exhibited a good rate capability and high reversible capacity of 700 mAh g^{-1} at a current density of 200 mA g^{-1} after 50 cycles. Given the synthetic convenience, scalability for quantity production, and better lithium storage property, we believe that the as-prepared porous Zn–Sn–O nanocubes could elicit widespread interest in lithium-ion batteries or other significant applications.

Acknowledgments This work is supported by the National Basic Research Program of China (2014CB239700), the Program of National Natural Science Foundation of China (21501120, 21371121 and 21331004), and Science and Technology Commission of Shanghai Municipality (14DZ1205700 and 14DZ2250800).

References

1. B. Scrosati, J. Garche, Lithium batteries: status, prospects and future. J. Power Sources **195**(9), 2419–2430 (2010). doi:10.1016/j.jpowsour.2009.11.048
2. J.-M. Tarascon, M. Armand, Issues and challenges facing rechargeable lithium batteries. Nature **414**(6861), 359–367 (2001). doi:10.1038/35104644

3. L. Ji, Z. Lin, M. Alcoutlabi, X. Zhang, Recent developments in nanostructured anode materials for rechargeable lithium-ion batteries. Energy Environ. Sci. **4**(8), 2682–2699 (2011). doi:10.1039/c0ee00699h
4. K. Kang, Y.S. Meng, J. Bréger, C.P. Grey, G. Ceder, Electrodes with high power and high capacity for rechargeable lithium batteries. Science **311**(5763), 977–980 (2006). doi:10.1126/science.1122152
5. M.S. Whittingham, Lithium batteries and cathode materials. Chem. Rev. **104**(10), 4271–4302 (2004). doi:10.1021/cr020731c
6. M. Winter, J.O. Besenhard, M.E. Spahr, P. Novak, Insertion electrode materials for rechargeable lithium batteries. Adv. Mater. **10**(10), 725–763 (1998). doi:10.1002/(SICI)1521-4095(199807)10:10<725:AID-ADMA725>3.0.CO;2-Z
7. Y. Idota, T. Kubota, A. Matsufuji, Y. Maekawa, T. Miyasaka, Tin-based amorphous oxide: a high-capacity lithium-ion-storage material. Science **276**(5317), 1395–1397 (1997). doi:10.1126/science.276.5317.1395
8. R. Wright, J. Christophersen, C. Motloch, J. Belt, C. Ho, V. Battaglia, J. Barnes, T. Duong, R. Sutula, Power fade and capacity fade resulting from cycle-life testing of advanced technology development program lithium-ion batteries. J. Power Sources **119–121**, 865–869 (2003). doi:10.1016/S0378-7753(03)00190-3
9. Y.G. Guo, J.S. Hu, L.J. Wan, Nanostructured materials for electrochemical energy conversion and storage devices. Adv. Mater. **20**(15), 2878–2887 (2008). doi:10.1002/adma.200800627
10. X.W.D. Lou, L.A. Archer, Z. Yang, Hollow micro-nanostructures: synthesis and applications. Adv. Mater. **20**(21), 3987–4019 (2008). doi:10.1002/adma.200800854
11. J. Jiang, Y. Li, J. Liu, X. Huang, C. Yuan, X.W.D. Lou, Recent advances in metal oxide-based electrode architecture design for electrochemical energy storage. Adv. Mater. **24**(38), 5166–5180 (2012). doi:10.1002/adma.201202146
12. F.-H. Du, K.-X. Wang, W. Fu, P.-F. Gao, J.-F. Wang, J. Yang, J.-S. Chen, A graphene-wrapped silver–porous silicon composite with enhanced electrochemical performance for lithium-ion batteries. J. Mater. Chem. A **1**(43), 13648–13654 (2013). doi:10.1039/c3ta13092d
13. J. Zai, K. Wang, Y. Su, X. Qian, J. Chen, High stability and superior rate capability of three-dimensional hierarchical SnS_2 microspheres as anode material in lithium ion batteries. J. Power Sources **196**(7), 3650–3654 (2011). doi:10.1016/j.jpowsour.2010.12.057
14. Y. Xiao, X. Li, J. Zai, K. Wang, Y. Gong, B. Li, Q. Han, X. Qian, $CoFe_2O_4$-graphene nanocomposites synthesized through an ultrasonic method with enhanced performances as anode materials for li-ion batteries. Nano-Micro Lett. **6**(4), 307–315 (2014). doi:10.1007/s40820-014-0003-7
15. X. Zhang, J. Ma, K. Chen, Impact of morphology of conductive agent and anode material on lithium storage properties. Nano-Micro Lett. **7**(4), 360–367 (2015). doi:10.1007/s40820-015-0051-7
16. J.S. Chen, X.W.D. Lou, SnO_2-based nanomaterials: synthesis and application in lithium-ion batteries. Small **9**(11), 1877–1893 (2013). doi:10.1002/smll.201202601
17. S. Ding, D. Luan, F.Y.C. Boey, J.S. Chen, X.W.D. Lou, SnO_2 nanosheets grown on graphene sheets with enhanced lithium storage properties. Chem. Commun. **47**(25), 7155–7157 (2011). doi:10.1039/c1cc11968k
18. Z. Wang, Z. Wang, W. Liu, W. Xiao, X.W.D. Lou, Amorphous $CoSnO_3$@C nanoboxes with superior lithium storage capability. Energy Environ. Sci. **6**(1), 87–91 (2013). doi:10.1039/C2EE23330D
19. Y. Chen, B. Qu, L. Mei, D. Lei, L. Chen, Q. Li, T. Wang, Synthesis of $ZnSnO_3$ mesocrystals from regular cube-like to sheet-like structures and their comparative electrochemical properties in Li-ion batteries. J. Mater. Chem. **22**(48), 25373–25379 (2012). doi:10.1039/c2jm33123c
20. A. Rong, X. Gao, G. Li, T. Yan, H. Zhu, J. Qu, D. Song, Hydrothermal synthesis of Zn_2SnO_4 as anode materials for Li-ion battery. J. Phys. Chem. B **110**(30), 14754–14760 (2006). doi:10.1021/jp062875r
21. G.-L. Xu, S.-R. Chen, J.-T. Li, F.-S. Ke, L. Huang, S.-G. Sun, A composite material of SnO_2 ordered mesoporous carbon for the application in Lithium-ion battery. J. Electroanal. Chem. **656**(1), 185–191 (2011). doi:10.1016/j.jelechem.2010.11.029
22. D. Larcher, S. Beattie, M. Morcrette, K. Edstroem, J.-C. Jumas, J.-M. Tarascon, Recent findings and prospects in the field of pure metals as negative electrodes for Li-ion batteries. J. Mater. Chem. **17**(36), 3759–3772 (2007). doi:10.1039/b705421c
23. X. Zhu, L. Geng, F. Zhang, Y. Liu, L. Cheng, Synthesis and performance of Zn_2SnO_4 as anode materials for lithium ion batteries by hydrothermal method. J. Power Sources **189**(1), 828–831 (2009). doi:10.1016/j.jpowsour.2008.07.028
24. L. Yuan, Z. Guo, K. Konstantinov, H.K. Liu, S. Dou, Nanostructured spherical porous SnO_2 anodes for lithium-ion batteries. J. Power Sources **159**(1), 345–348 (2006). doi:10.1016/j.jpowsour.2006.04.048
25. L. Li, X. Yin, S. Liu, Y. Wang, L. Chen, T. Wang, Electrospun porous SnO_2 nanotubes as high capacity anode materials for lithium ion batteries. Electrochem. Commun. **12**(10), 1383–1386 (2010). doi:10.1016/j.elecom.2010.07.026
26. M. Marcinek, L. Hardwick, T. Richardson, X. Song, R. Kostecki, Microwave plasma chemical vapor deposition of nano-structured Sn/C composite thin-film anodes for Li-ion batteries. J. Power Sources **173**(2), 965–971 (2007). doi:10.1016/j.jpowsour.2007.08.084
27. Z. Wen, Q. Wang, Q. Zhang, J. Li, In situ growth of mesoporous SnO_2 on multiwalled carbon nanotubes: a novel composite with porous-tube structure as anode for lithium batteries. Adv. Funct. Mater. **17**(15), 2772–2778 (2007). doi:10.1002/adfm.200600739
28. Y. Wang, H.C. Zeng, J.Y. Lee, Highly reversible lithium storage in porous SnO_2 nanotubes with coaxially grown carbon nanotube overlayers. Adv. Mater. **18**(5), 645–649 (2006). doi:10.1002/adma.200501883
29. X.M. Yin, C.C. Li, M. Zhang, Q.Y. Hao, S. Liu, L.B. Chen, T.H. Wang, One-step synthesis of hierarchical SnO_2 hollow nanostructures via self-assembly for high power lithium ion batteries. J. Phys. Chem. C **114**(17), 8084–8088 (2010). doi:10.1021/jp100224x
30. H. Kim, J. Cho, Hard templating synthesis of mesoporous and nanowire SnO_2 lithium battery anode materials. J. Mater. Chem. **18**(7), 771–775 (2008). doi:10.1039/b714904b
31. M. Xu, F. Wang, M. Zhao, S. Yang, X. Song, Molten hydroxides synthesis of hierarchical cobalt oxide nanostructure and its application as anode material for lithium ion batteries. Electrochim. Acta **56**(13), 4876–4881 (2011). doi:10.1016/j.electacta.2011.03.027
32. C. Wang, Y. Zhou, M. Ge, X. Xu, Z. Zhang, J. Jiang, Large-scale synthesis of SnO_2 nanosheets with high lithium storage capacity. JACS **132**(1), 46–47 (2009). doi:10.1021/ja909321d
33. H. Wang, Q. Pan, Y. Cheng, J. Zhao, G. Yin, Evaluation of ZnO nanorod arrays with dandelion-like morphology as negative electrodes for lithium-ion batteries. Electrochim. Acta **54**(10), 2851–2855 (2009). doi:10.1016/j.electacta.2008.11.019
34. N. Feng, S. Peng, X. Sun, L. Qiao, X. Li, P. Wang, D. Hu, D. He, Synthesis of monodisperse single crystal Zn_2SnO_4 cubes with high lithium storage capacity. Mater. Lett. **76**, 66–68 (2012). doi:10.1016/j.matlet.2012.02.071
35. X.W. Lou, Y. Wang, C. Yuan, J.Y. Lee, L.A. Archer, Template-free synthesis of SnO_2 hollow nanostructures with high lithium

storage capacity. Adv. Mater. **18**(17), 2325–2329 (2006). doi:10.1002/adma.200600733
36. S. Han, B. Jang, T. Kim, S.M. Oh, T. Hyeon, Simple synthesis of hollow tin dioxide microspheres and their application to lithium-ion battery anodes. Adv. Funct. Mater. **15**(11), 1845–1850 (2005). doi:10.1002/adfm.200500243
37. L.-S. Zhang, L.-Y. Jiang, H.-J. Yan, W.D. Wang, W. Wang, W.-G. Song, Y.-G. Guo, L.-J. Wan, Mono dispersed SnO_2 nanoparticles on both sides of single layer graphene sheets as anode materials in Li-ion batteries. J. Mater. Chem. **20**(26), 5462–5467 (2010). doi:10.1039/c0jm00672f
38. M. Ahmad, S. Yingying, A. Nisar, H. Sun, W. Shen, M. Wei, J. Zhu, Synthesis of hierarchical flower-like ZnO nanostructures and their functionalization by Au nanoparticles for improved photocatalytic and high performance Li-ion battery anodes. J. Mater. Chem. **21**(21), 7723–7729 (2011). doi:10.1039/c1jm10720h
39. H. Liu, D. Su, R. Zhou, B. Sun, G. Wang, S.Z. Qiao, Highly ordered mesoporous MoS_2 with expanded spacing of the (002) crystal plane for ultrafast lithium ion storage. Adv. Energy Mater. **2**(8), 970–975 (2012). doi:10.1002/aenm.201200087